Appendix 1. Synchrotron experiments

X-ray scattering experiments were performed at the TRUSAXS instrument of the European Synchrotron Radiation Facility (ESRF), Grenoble, France (beamline ID-02). In this beamline, the sample-to-detector distance (SDD) for SAXS experiments ranges between 0.8m and 31m, offering a unique setup for studying a broad range of length scales ($0.002<q<50\ nm^{-1}$).

During acquisition, two simultaneous detectors allowed for SAXS/WAXS or USAXS/WAXS measurements (Figure A1.A). The WAXS detector was a Rayonix LX 170HS (Rayonix, Evanston, USA), while the SAXS/USAXS detector was an EIGER2-4M (commercially available from Dectris, Baden, Switzerland). The latter was placed on a motorized wagon rail, allowing to change the SAXS SDD [1] (Figure A1.B). Each experiment was repeated twice, once with simultaneous SAXS and WAXS (SDD 2 m and 0.14 m) and once with simultaneous USAXS and WAXS (SDD 31 m and 0.14 m). Before measurement, a calibration was performed using aluminum oxide Al2O3 for the WAXS detector. Silver behenate and polystyrene beads of 2 µm were used to validate the distance in SAXS and USAXS (silver behenate was used at 0.8m, while polystyrene was used at 10 and 31m). A calibrated transmission diode was used to measure the transmitted flux.

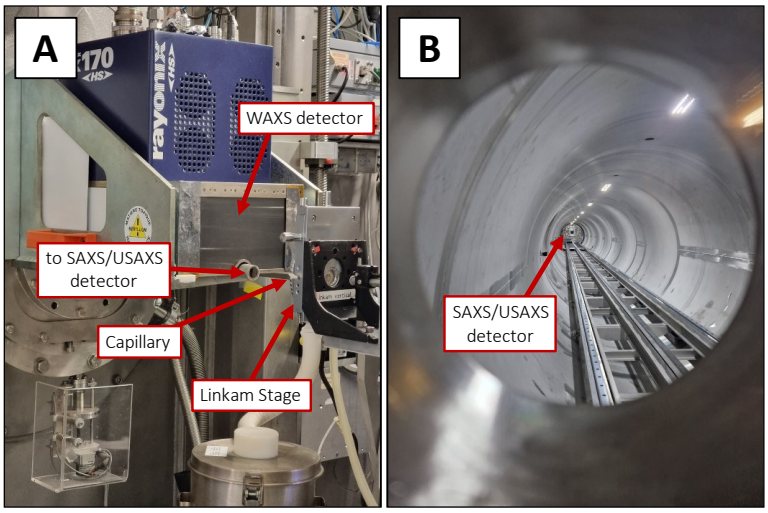

Figure A 1. Pictures of the experimental setup in ID02. In panel A, it is possible to visualize the Linkam stage, which is used for temperature control. The capillary containing the sample is placed on the stage for acquisition. The two simultaneous detectors are also visible (WAXS and SAXS/USAXS). Figure B shows the length of the beamline tunnel, allowing for a long SDD.

During measurement, samples were placed in a temperature-controlled stage equipped with a Peltier element capillary holder controlled by a 5R6-900 benchtop temperature controller (Oven Industries, Camp Hill, USA) set at 15°C. One time acquisition of 0.1s was performed in each sample (10 frames per acquisition). For the capillaries, sample thickness was measured by means of a transmission scan.

In each acquisition, two-dimensional patterns were recollected and normalized to an absolute intensity scale using the standard procedure (for WAXS: dark image subtraction, flatfield, polarization and solid angle correction, transmitted intensity correction; for SAXS: flatfield, solid angle and transmitted intensity correction).[2] The two-dimensional images were then reduced to 1D profiles by means of an azimuthal integration. The scattering intensity (I(q)) was plotted against the scattering vector q, defined in Equation A1, where θ is the scattering angle and λ is the x-ray wavelength (1.013 Å).[2] The units of scattering vector q are thus inverse length. The ten frames per acquisition were averaged to obtain a one-dimensional scattering profile. An empty capillary was used as a background, and the collected 1D pattern was subtracted from each acquisition to correct for sample holder and background (empty beam, capillary and air gap). The software SAXSutilities was utilized for averaging and subtraction.[3, 4] Using the same software, the SAXS-USAXS curves were merged scaling for the high q-data. The marge region ranged was between 0.0826 nm^{-1} to 0.1903 nm^{-1} . Each sample was divided by the measured sample thickness (capillary diameter) to obtain the intensity in absolute scale (in mm^{-1}). For the fits, a dynamic rebin was performed to arrange the points homogeneously on a logarithmic q scale (SAXSutilities).[3, 4]

$$q = \left(\frac{4\pi}{\lambda}\right) sin\left(\frac{\theta}{2}\right) \qquad \text{[Equation A1]}$$

The q range was between 0.0018 and 0.2453 nm^{-1} for the USAXS results, 0.0351 to 4.5055 nm^{-1} for the SAXS results and in between 5.3990 and 39.3967 nm^{-1} for the WAXS results (Figure A2). Therefore, the maximum recorded distance corresponds to 3.49 µm.

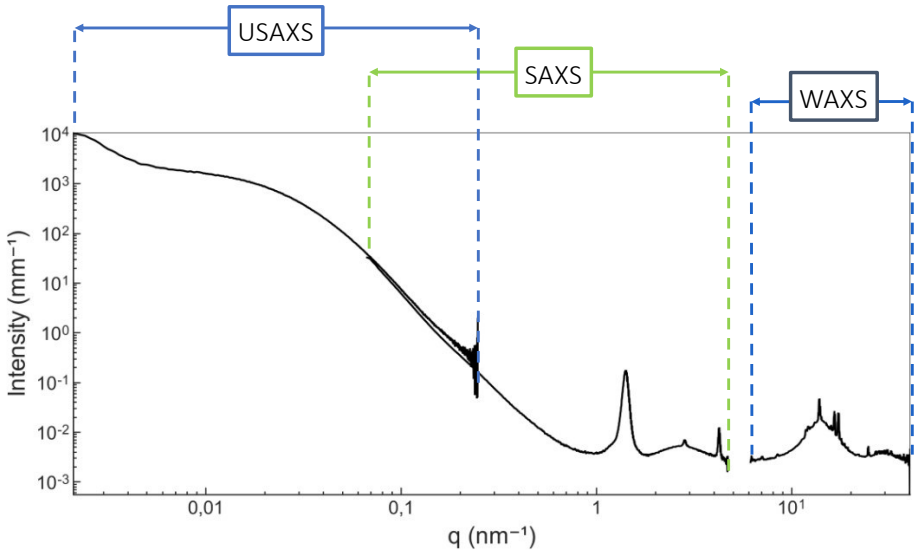

Figure A 2. Overview of the q-ranges acquired with different sample to detector distance (WAXS, SAXS and USAXS).

Appendix 2. Structure of Triglycerides in the β form

The crystallographic arrangement of triglyceride molecules has been extensively characterized. In 1998, van Langevelde et al. presented, the 3D arrangement of saturated monoacid triglycerides in the β phase in great level of detail.[5] Figure A3 presents a simplified 3D diagram of the crystalline structure.

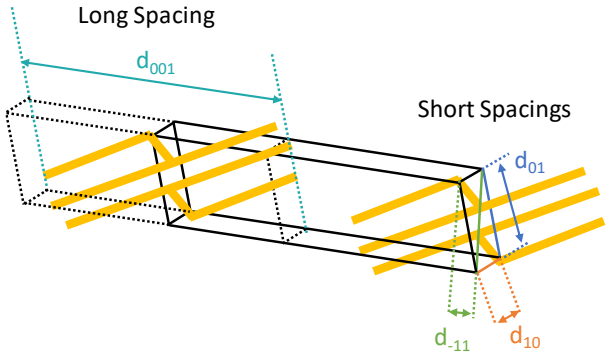

Figure A 3. Graphical representation of the 3D structure of saturated monoacid triglycerides. In yellow, four different saturated monoacid triglycerides. The unit cell is presented in black filled lines. Although four molecules are presented to visualize the TAG stacking, there are only two TAG molecules per unit cell. Dotted lines indicate projections. The representation is the combined adaptation from the other references[5-7].

As seen in Figure A3, the unit cell in the β phase is characterized by a triclinic arrangement. The calculation of area per chain has been recently described by Tenorio-Garcia et al,[6] and is presented in equation A2. In summary, the authors claim that the cross-section of the triclinic projection can be described as the summation of two identical triangles (see Figure A4, one triangle is denoted as abc). By knowing the three different short spacings (d_{10}, d_{-11} and d_{01}), the height of the triangle is known and the area can be determined by applying Heron's formula.

$$A_C^{\beta} = \frac{2d_{10}^2 d_{-11}^2 d_{01}^2}{\sqrt{(d_{10}\,d_{-11} + d_{-11}d_{01} + d_{01}d_{10})(-d_{10}d_{-11} + d_{-11}d_{01} + d_{01}d_{10})(d_{10}d_{-11} - d_{-11}d_{01} + d_{01}d_{10})(d_{10}d_{-11} + d_{-11}d_{01} - d_{01}d_{10})}} \quad \text{[Equation A2]}$$

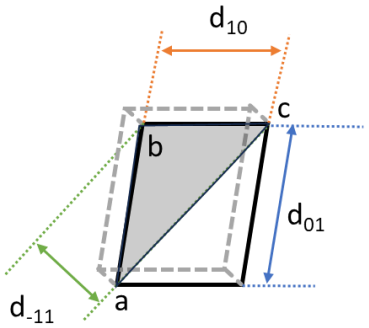

Figure A 4. Representation of the triclinic arrangement. The area per chain can be determined by obtaining the indexes d01, d10, d-11, which specify the heights of the triangle abc.

Appendix 3. Long Spacing Calculations

In order to calculate the long spacings, a three step procedure was utilized.

1. First, the baseline of the oil was subtracted to the profile (Figure A3). For this, a polynomial function was utilized.

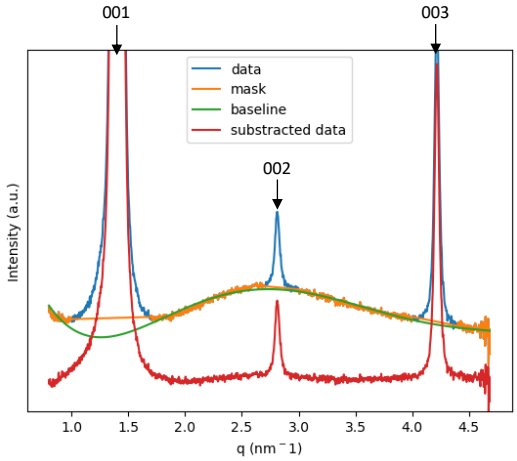

Figure A5. Example of the steps followed to performed an oil baseline subtraction. First, a mask is selected to remove the peaks from the baseline. Then, the baseline is fitted to a polynomial function. Finally, the resulting function is subtracted from the sample. In this example, a 30% SSS sample, crystallized at 1°C/min until 15°C.

2. Each peak was fitted to a Gaussian curve and the peak position and full width at half maximum (FWHM) were calculated for the three available peak reflections (001, 002 and 003) (Figure A4).

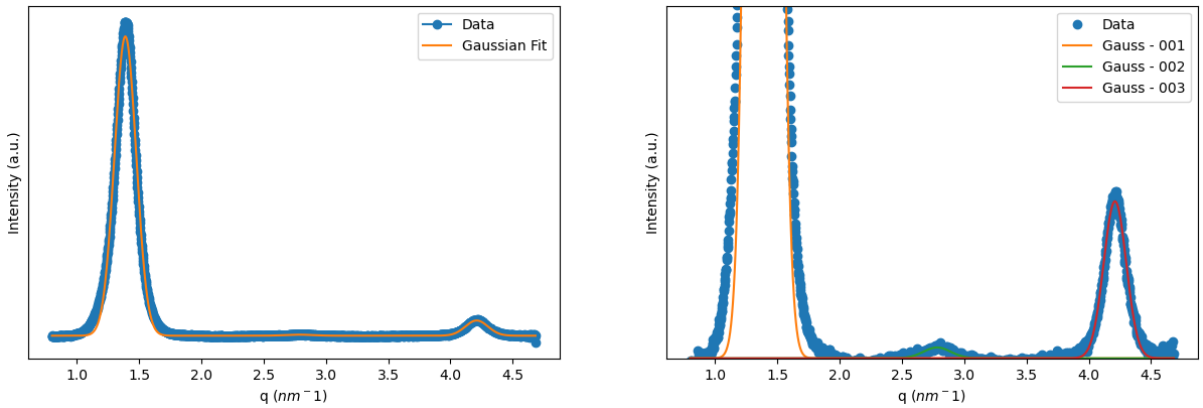

Figure A6. Peak fitting procedure. For this, each reflection is fitted to a gaussian bell function. In this example, a 30% FHRO sample, crystallized at 10°C/min until 15°C was utilized.

3. The recorded peak positions were plotted against Miller index (Figure A5). A linear regression was performed assuming an intercept at 0 (which always reported $R^2 \approx 1$) and the intercept (m) was obtained. The slope was utilized to determine Domain size following Equation A2.

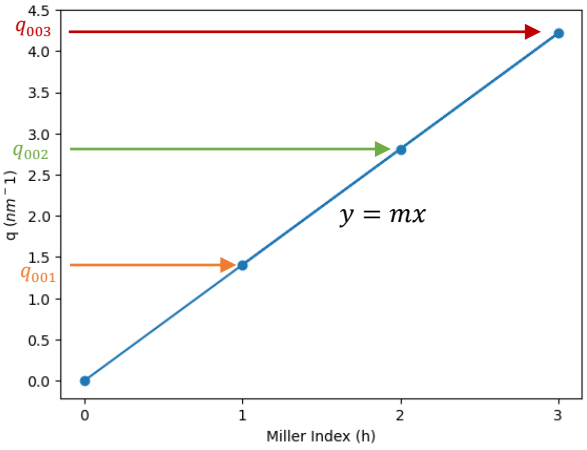

Figure A7. Miller index vs q. The slope of the plot was calculated to determine domain size. In this example, a 30% FHRO sample, crystallized at 10°C/min until 15°C was utilized.

$$\boldsymbol{Domain\ Size} = \frac{2\pi}{m} \qquad \text{[Equation A3]}$$

Appendix 4. Crystallite thickness distribution - Bertaut–Warren–Averbach method (BWA)

The first-order SAXS peak (001) was utilized to obtain a crystallite thickness distribution (CDT). The methodology utilized has been previously described by Rondou et al,.[8], with the exception of a minor modification. After baseline subtraction, the resulting curve was converted into a new distribution s^*, where the center of the distribution is at $s^* = 0$, and the tails ranged between $s^* = -1/2$ and $s^* = 1/2$. The s^* curve was then deconvoluted into a sum of Gaussian bells. This step assumes that the SAXS peak results from the summation of different d-spacings. A large number of terms (25) are utilized to avoid oversimplification of the SAXS curve and to avoid presumptions about the shape of the distribution. The summation of those curves was then normalized into $\phi(s^*)$. The remaining procedure remains unchanged, and follows the steps described elsewhere.[8] A MATLAB R2021b script was utilized to perform all the calculations.

Appendix 5. Williamson-Hall Plot

To calculate micro strain, a Williamson-Hall plot was utilized. As explained in Equation 5, the slope is equal to the strain, while the intercept is equal to $K\lambda/D_{WH}$.

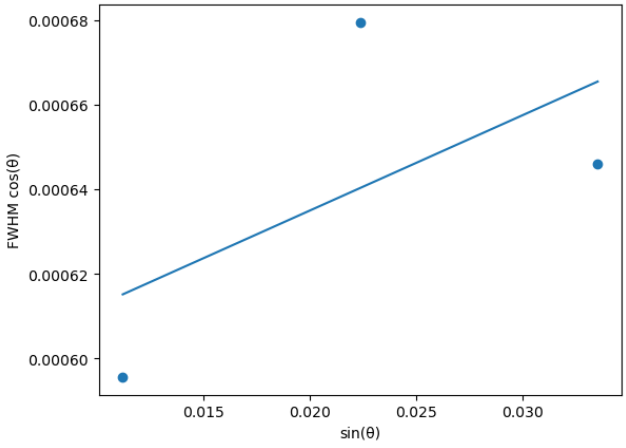

Figure A8. Example of a Williamson-Hall plot utilized for micro strain and size domain termination determination. In the context of this research, only the SAXS reflections were utilized. In this example, a 30% SSS sample, crystallized at 1°C/min until 15°C was utilized.

Appendix 6. Instrumental peak broadening

Instrumental peak broadening is traditionally attributed to a sum of factors, including detector resolution broadening, beam size broadening, wavelength broadening and beam divergence. The measured peak is therefore a convoluted contribution of specimen and instrumental broadening. Assuming a gaussian shape, the measured FWHM ($\mathrm{FHWM_M}$) can be expressed as the summation of the squares of full width height maximum of the sample ($\mathrm{FWHM_S}$) plus squared instrumental peak broadening (dq) (Equation A8).

$$\mathrm{FWHM_M} = \sqrt{\mathrm{FWHM_S^2} + \mathrm{dq^2}} \qquad \text{[Equation A4]}$$

Based on previous standard experiments on the same beamline, instrumental peak broadening dq was estimated to be in the order of 6x10^{-3} nm^{-1} for the utilized SAXS range (using a sample to detector distance of 1.41 m). Table A1 illustrates the impact of instrumental peak broadening in the crystallite size. For all samples, the difference was found to be below nanometer scale and therefore was considered, for the purpose of this research, negligible.

Table A1. Effect of instrumental peak broadening on the determination of crystallite size utilizing the Scherrer equation.

Sample	Measured FWHM	Corrected FWHM	Scherrer crystallite size without correction	Scherrer crystallite size with correction	Difference
Units	(nm^{-1})	(nm^{-1})	(nm)	(nm)	(nm)
30% SSS – 10°C/min	0.122	0.122	46.391	46.447	5.63E-02
30% SSS – 1°C/min	0.075	0.075	75.550	75.794	2.44E-01
30% FHRO – 10°C/min	0.287	0.287	19.686	19.691	4.30E-03
30% FHRO - Pilot Scale	0.290	0.290	19.509	19.513	4.18E-03

Appendix 7. CNP aspect ratio

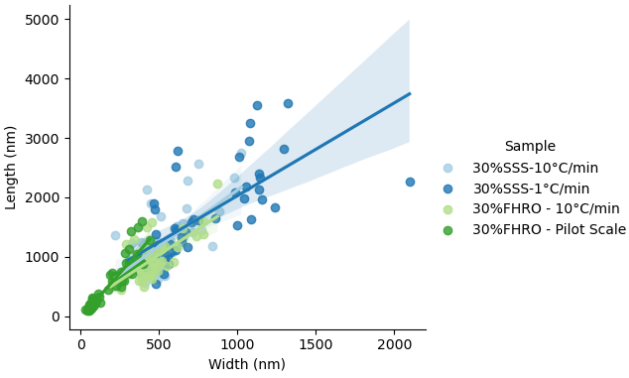

Figure A9. Scatter plots of the length and width of CNPs, grouped by sample. A linear regression is presented to visualize changes in aspect ratio between treatments. All treatments have very comparable regression slopes, suggesting similar length to width ratios. Small deviations in the ratio are visible for the Pilot Scale sample. L/W median ratios are 0.47 for the 30%SSS – 10°C/min, 0.48 for the 30%SSS – 1°C/min, 0.49 for the 30%FHRO – 10°C/min and finally 0.38 for the Pilot Scale 30%FHRO.

Appendix 8. USAXS Models

Appendix 8A. Unified Fit

Also known as the unified scattering function, it was first proposed by Beaucage in 1994.[9] The underlying principle behind it suggests that in multi-level systems, the scattering function can be described as the empirical summation of multiple Guinier regions and their associated power-law regimes.[9] In this context, a structural level is considered as a group of similar scattering units that share a length scale. Scatterers can thus be the basic scattering units or the aggregates of those units. Equation A8 describes the Unified Fit model where P is the Porod exponent, which provides information on the conformation of the scatterers; R_g is the radius of gyration that provides information on the average size of the scatterers. G and B are known to be Guinier-Porod scale factors; the subscript i indicates a particular structural level, while i+1 indicates the next structural level and erf is the error function.[9, 10]

$$I(q) \approx \sum_{i=1}^{n} G_i \exp\left(-\frac{q^2 R_{g_i}^2}{3}\right) + \mathrm{B}_i \exp\left(-\frac{q^2 R_{g_{i+1}}}{3}\right) \times \left[\frac{\left(\mathrm{erf}\left(qR_{\mathrm{g_i}}/\sqrt{6}\right)\right)^3}{q}\right]^{P_i}$$

[Equation A5]

When assuming a spherical scatterer, the R_g is linked to the average CNP radius R, by Equation A10.[11]

$$R_g^2 = \frac{3\langle R^8\rangle}{5\langle R^6\rangle}$$

[Equation A6]

In the research of Peyronel et al., Equation A9 is simplified to Equation A11.[9, 12] This transformation assumes monodisperse spherical scatterers.

$$R = \sqrt{\frac{5}{3}} R_g$$

[Equation A7]

Appendix 8B. Guinier-Porod Fit

The Guinier-Porod model, developed by Hammouda,[13] overcomes some of the deficiencies of the Unified Fit model. The model includes an s-factor, which accounts for shape deviations (Equation 10). In the context of 3D globular objects, such as spheres, s assumes a value of 0. For 2D symmetry, as observed in rod-like structures, s equals 1, and for 1D symmetry, such as lamellae or platelets, s is assigned a value of 2.[13]

$$I(q) = \begin{cases} \frac{B}{q^P} & q \geq q_1 \\ \frac{G_1}{q^{s_1}} e^{\left(-\frac{q^2 R_{g_1}^2}{3-s_1}\right)} & q_2 \leq q \leq q_1 \\ \frac{G_2}{q^{s_2}} e^{\left(-\frac{q^2 R_{g_2}^2}{3-s_2}\right)} & q \leq q_2 \end{cases}$$

[Equation A8]

Appendix 9. Scattering of oil phase (USAXS range)

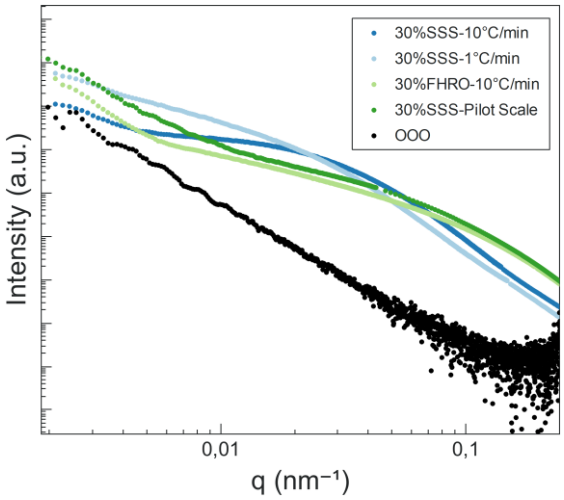

Figure A 10. USAXS results (I vs q) including a sample of 100% triolein. As seen in the image, the oil contribution remains always bellow the contribution of the crystallized systems. Therefore, the scattering contribution of the oil was considered negligible in the USAXS range.

Appendix 10.Sensitivity Analysis

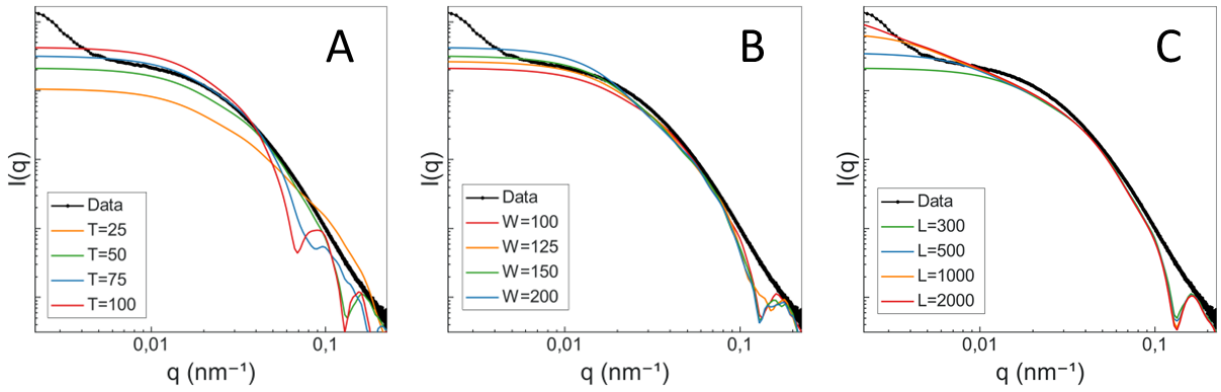

Figure A 11. Sensitivity analysis of a parallelepiped model, following the equation $I(q) = scale \cdot (\Delta\rho)^2 \cdot \langle P_{PP} \rangle$. *In each plot, one factor was systematically changed, and the resulting model was plotted. Panel A illustrates variations in thickness (T), Panel B captures alterations in width (W), and Panel C examines the effects of changes in length (L).*

Appendix 11. Polydispersity

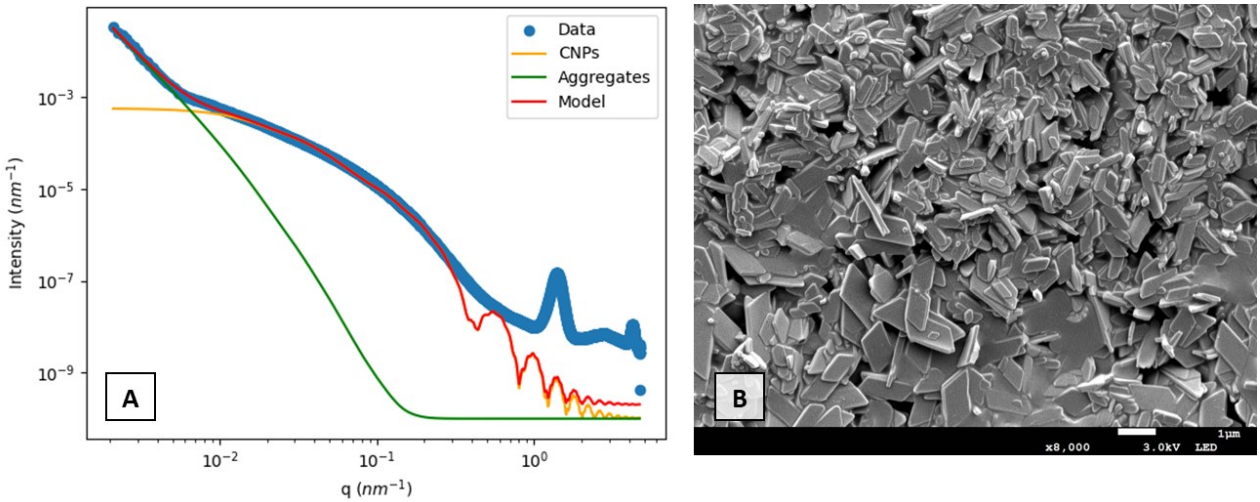

Figure A 12. (A) A fit not including polydispersity. In this case, a deviation from the experimental data is observed at high-q. (B) Cryo-SEM microscopy with a clear size variability. This image support the polydispersity assumptions.

References

1. Narayanan, T.; Sztucki, M.; Van Vaerenbergh, P.; Leonardon, J.; Gorini, J.; Claustre, L.; Sever, F.; Morse, J.; Boesecke, P., A multipurpose instrument for time-resolved ultra-small-angle and coherent X-ray scattering. *J Appl Crystallogr* 2018, *51* (Pt 6), 1511-1524.
2. Narayanan, T.; Sztucki, M.; Van Vaerenbergh, P.; Léonardon, J.; Gorini, J.; Claustre, L.; Sever, F.; Morse, J.; Boesecke, P., A multipurpose instrument for time-resolved ultra-small-angle and coherent X-ray scattering. *J Appl Crystallogr* 2018, *51*, 1511-1524.
3. Narayanan, T.; Sztucki, M.; Zinn, T.; Kieffer, J.; Homs-Puron, A.; Gorini, J.; Van Vaerenbergh, P.; Boesecke, P., Performance of the time-resolved ultra-small-angle X-ray scattering beamline with the Extremely Brilliant Source. *J Appl Crystallogr* 2022, *55* (1), 98-111.
4. Michael, S., SAXSutilities: a graphical user interface for processing and analysis of Small-Angle X-ray Scattering data 1.024 ed.; Zenodo, 2011.
5. Van Langevelde, A.; Van Malssen, K.; Hollander, F.; Peschar, R.; Schenk, H., Structure of mono-acid even-numbered β-triacylglycerols. *Acta Crystallographica Section B* 1999, *55* (1), 114-122.
6. Tenorio-Garcia, E.; Araiza-Calahorra, A.; Rappolt, M.; Simone, E.; Sarkar, A., Pickering Water-in-Oil Emulsions Stabilized Solely by Fat Crystals. *Advanced Materials Interfaces* 2023, *10* (31).
7. van Langevelde, A.; van Malssen, K.; Hollander, F.; Peschar, R.; Schenk, H., CCDC 131755: Experimental Crystal Structure Determination. 12/03/1999 ed.; CDCC, 1999.
8. Rondou, K.; De Witte, F.; Rimaux, T.; Dewinter, W.; Dewettinck, K.; Verwaeren, J.; Van Bockstaele, F., Multiscale analysis of monoglyceride oleogels during storage. *Journal of the American Oil Chemists' Society* 2022, *99* (11), 1019-1031.
9. Beaucage, G., Approximations leading to a unified exponential power-law approach to small-angle scattering. *J Appl Crystallogr* 1995, *28*, 717-728.
10. Peyronel, F.; Pink, D. A., Ultra-Small Angle X-ray Scattering. In *Structure-Function Analysis of Edible Fats*, 2018; pp 267-285.
11. Beaucage, G.; Kammler, H. K.; Pratsinis, S. E., Particle size distributions from small-angle scattering using global scattering functions. *J Appl Crystallogr* 2004, *37* (4), 523-535.
12. Peyronel, F.; Ilavsky, J.; Mazzanti, G.; Marangoni, A. G.; Pink, D. A., Edible oil structures at low and intermediate concentrations. II. Ultra-small angle X-ray scattering of in situ tristearin solids in triolein. *J Appl Phys* 2013, *114* (23).
13. Hammouda, B., A new Guinier–Porod model. *J Appl Crystallogr* 2010, *43* (4), 716-719.